Photon ring and observational appearance of a hairy black hole

Qingyu Gan,[*] Peng Wang,[†] Houwen Wu,[‡] and Haitang Yang[§]
Center for Theoretical Physics, College of Physics, Sichuan University, Chengdu 610064, China

(Received 5 July 2021; accepted 28 July 2021; published 18 August 2021)

Recently, the image of a Schwarzschild black hole with an accretion disk has been revisited, and it showed that the "photon ring," defined as highly bent light rays that intersect the disk plane more than twice, is extremely narrow and makes a negligible contribution to the total brightness. In this paper, we investigate the observational appearance of an optically and geometrically thin accretion disk around a hairy black hole in an Einstein-Maxwell-scalar model. Intriguingly, we find that in a certain parameter regime, due to an extra maximum or an "anklelike" structure in the effective potential for photons, the photon ring can be remarkably wide, thus making a notable contribution to the flux of the observed image. In particular, there appears a wide and bright annulus, which comprises multiple concentric bright thin rings with different luminosity, in the high resolution image.

DOI: 10.1103/PhysRevD.104.044049

I. INTRODUCTION

The announcement of the first angular resolution image of the supermassive black hole M87* by the Event Horizon Telescope (EHT) collaboration is a significant event in observing astrophysical black holes [1–8] which opens a new window to test general relativity in the strong field regime. The image contains two prominent features, a circular dark interior, dubbed "shadow," and a bright ring which is closely relevant to a class of circular photon orbits (i.e., photon sphere). The shadow and photon sphere are originated from the light deflection by the strong gravitational field near the black hole [9–12]. Thus, it is believed that the shadow image encodes valuable information of the geometry around the black hole, especially in the vicinity of the horizon.

Modeling the M87* with the Kerr black hole geometry, the observation was found to be in good agreement with the prediction of general relativity. Nevertheless, due to the finite resolution of the M87* image, there still exists some space for alternative models to simulate the black hole image within observational uncertainty tolerance. To explore these possibilities, one can parametrize the deviations from the Kerr metric and compare the corresponding shadow image with the observed image [13–18]. Alternatively, shadows and photon spheres of black holes are widely studied in the context of various specific theories including new physics, e.g., the nonlinear electrodynamics [19–23], the Gauss-Bonnet theory [24–27], fuzzball [28], the Chern-Simons-type theory [29,30], $f(R)$ gravity [31,32], and string inspired black holes [33–36]. Moreover, there could exist some exotic ultracompact objects acting as black hole mimickers [37]. The gravitational lensing by various horizonless objects, such as wormholes [38–40] and bosonic stars [41,42], has been detailedly analyzed. Their shadow images are usually distinct from those of black holes, but it is hard to distinguish between them at the current EHT resolution. Interestingly, it was argued in [43–45] that naked singularities can cast a shadow in the absence of the photon sphere. Furthermore, the EHT observation can also be applied to impose constraints on the cosmological parameters [46–51] and the size of extra dimensions [52–54], test the equivalence principle [55–57], and probe some fundamental physics issues including dark matter [21,58–63] and dark energy [64–67].

On the other hand, an astrophysical black hole is generally believed to be surrounded by a luminous accretion flow, which is an essential ingredient in obtaining the black hole image. In fact, the realistic image is a result of the complex interactions between the strong gravitational lensing of the black hole and the electromagnetic plasma in the accretion flow, which requires intensive numerical general relativistic magnetohydrodynamic simulations [68]. Nevertheless, simplified accretion models usually suffice to capture major features of black hole images, and hence have been widely investigated in the literature, e.g., spherical accretion flows [26,43,63,65,66,69], thin or thick accretion disks [70–77]. In particular, Gralla *et al.* [72] considered the emission from an optically and geometrically thin disk lying in the equatorial plane of a Schwarzschild black hole, which is divided into three classes by the number m of half orbits that an emitted

[*]gqy@stu.scu.edu.cn
[†]pengw@scu.edu.cn
[‡]iverwu@scu.edu.cn
[§]hyanga@scu.edu.cn

photon completes around the black hole before reaching a distant observer at the "north pole": the direct emission ($m \leq 1$), the lensing ring ($m = 2$), and the photon ring ($m \geq 3$). The results in [72] show that the lensing ring superimposed upon the direct emission produces a thin ring of twice the background intensity in the black hole image, while the photon ring, which picks up larger intensity, makes negligible contributions to the total observed brightness due to its exponential narrowness. Nevertheless, observations of the photon ring would provide a new and powerful tool to probe a black hole spacetime [78]. Recently, experimental methods have been proposed to detect the photon ring by measuring its interferometric signatures [79] and two-point correlation function of intensity fluctuations [80].

The no-hair theorem states that a black hole can be completely characterized by only three observable classical parameters: mass, electric charge, and spin [81]. However, various models of hairy black holes (HBHs) have been proposed to circumvent the no-hair theorem (see [82] for a review). Testing the no-hair theorem with observations would provide powerful probes of alternative theories of gravity. The observation of the black hole shadow would enable tests of the no-hair theorem, and therefore studying shadows of HBHs with various hairs has attracted great attention, e.g., axionlike hairs [83,84], dilatonlike hairs [85–87], and others [88–94]. Interestingly, in [95] we found that there can exist two unstable photon spheres outside the event horizon for the HBH solutions in the Einstein-Maxwell-scalar (EMS) theory proposed in [96]. This novel feature results in two concentric bright rings of different radii in the observed image of the HBH surrounded by an optically thin, spherical accretion flow. Note that the presence of more than one photon sphere has also been reported in other scenarios, e.g., horizonless ultracompact objects [97], Morris-Thorne-type wormholes [38,98], reflection-asymmetric wormholes [39,40,99,100], and a Schwarzschild black hole surrounded by a certain matter distribution [101].

To investigate the effects of two unstable photon spheres on the photon ring, we consider the observational appearance of the aforementioned HBH surrounded by an optically and geometrically thin accretion disk. Remarkably, we show that, in a certain parameter regime, the existence of two photon spheres or its reminiscence can significantly extend the photon ring band, which thus makes a nontrivial contribution to the total observed intensity, comparable to that of the lensing ring. The rest of the paper is organized as follows. In Sec. II, we briefly review the HBH solutions, the behavior of null geodesics, and the observed intensity of the accretion disk. Section III contains our main numerical results, which include effective potentials for photons, accretion disk images seen by a distant observer, and the dependence of the photon ring on the HBH charge and scalar coupling. We conclude with a brief discussion in Sec. IV. We set $16\pi G = 1$ throughout the paper.

II. SETUP

Consider a specific 4D EMS theory with an exponential scalar-electromagnetic coupling given by [96]

$$S = \int d^4x\sqrt{-g}[\mathcal{R} - 2\partial_\mu\phi\partial^\mu\phi - e^{\alpha\phi^2}F_{\mu\nu}F^{\mu\nu}], \quad (1)$$

where $\mathcal{R}$ is the Ricci scalar, the scalar field ϕ is minimally coupled to the metric $g_{\mu\nu}$ and nonminimally coupled to the electromagnetic field A_μ, and $F_{\mu\nu} = \partial_\mu A_\nu - \partial_\nu A_\mu$ is the electromagnetic tensor. Many properties of this model and its extensions have been explored in the literature, e.g., various nonminimal coupling functions [102,103], dyons including magnetic charges [104], axionic-type couplings [105], massive and self-interacting scalar fields [106,107], horizonless reflecting stars [108], stability analysis of the HBHs [109–113], higher-dimensional scalar-tensor models [114], quasinormal modes of the HBHs [115,116], two U(1) fields [117], quasitopological electromagnetism [118], topology and spacetime structure influences [119], the Einstein-Born-Infeld-scalar theory [120], and with a negative cosmological constant [121,122]. Starting with the static and spherically symmetric black hole solution ansatz,

$$ds^2 = -N(r)e^{-2\delta(r)}dt^2 + \frac{dr^2}{N(r)} + r^2(d\theta^2 + \sin^2\theta d\varphi^2),$$
$$\mathbf{A} = A_t dt = V(r)dt, \quad (2)$$

we obtain the equations of motion

$$2m'(r) - r^2N(r)\phi'(r)^2 - e^{2\delta(r)+\alpha\phi(r)^2}r^2V'(r)^2 = 0,$$
$$\delta'(r) + r\phi'(r)^2 = 0,$$
$$[e^{-\delta(r)}r^2N(r)\phi'(r)]' - \alpha e^{\delta(r)+\alpha\phi(r)^2}\phi(r)r^2V'(r)^2 = 0,$$
$$[e^{\delta(r)+\alpha\phi(r)^2}r^2V'(r)]' = 0, \quad (3)$$

where $N(r) \equiv 1 - 2m(r)/r$ can be expressed in terms of the Misner-Sharp mass function $m(r)$, and primes denote derivatives with respect to r. The last equation in Eq. (3) yields $V'(r) = -e^{-\delta(r)-\alpha\phi(r)^2}Q/r^2$, where the constant Q can be interpreted as the electric charge of the black hole. To solve the above nonlinear ordinary differential equations, suitable boundary conditions at the event horizon of radius r_h and spatial infinity shall be imposed as

$$m(r_h) = \frac{r_h}{2}, \quad \delta(r_h) = \delta_0, \quad \phi(r_h) = \phi_0, \quad V(r_h) = 0,$$
$$m(\infty) = M, \quad \delta(\infty) = 0, \quad \phi(\infty) = 0, \quad V(\infty) = \Psi, \quad (4)$$

where δ_0 and ϕ_0 are two positive constants, M is the Arnowitt-Deser-Misner mass, and Ψ is the electrostatic potential. The scalar-free black hole solution with $\phi = 0$ corresponds to Reissner-Nordström black holes (RNBHs). When the dimensionless coupling α is larger than $1/4$, there exist HBH solutions with a nontrivial profile of the scalar field $\phi(r)$ [96,102,120]. In this paper, we focus on the fundamental state of the HBH solutions, which means that $\phi(r)$ remains positive outside the event horizon.

The behavior of a photon traveling outside the HBH can be encapsulated in the null geodesic equation,

$$\frac{d^2x^\mu}{d\lambda^2} + \Gamma^\mu_{\rho\sigma}\frac{dx^\rho}{d\lambda}\frac{dx^\sigma}{d\lambda} = 0, \tag{5}$$

where λ is the affine parameter and $\Gamma^\mu_{\rho\sigma}$ is the Christoffel symbol. In the Appendix, we show that light rays propagating in the HBH spacetime indeed are determined by the null geodesic equation. Due to the spherical symmetry, we only consider light rays moving on the equatorial plane with $\theta = \pi/2$. Combining $ds^2 = 0$ and Eqs. (2) and (5), one obtains the time, azimuthal, and radial components of the null geodesic,

$$\begin{aligned}\frac{dt}{d\lambda} &= \frac{1}{bN(r)e^{-2\delta(r)}},\\ \frac{d\varphi}{d\lambda} &= \pm\frac{1}{r^2},\\ e^{-2\delta(r)}\left(\frac{dr}{d\lambda}\right)^2 &= \frac{1}{b^2} - \frac{e^{-2\delta(r)}N(r)}{r^2},\end{aligned} \tag{6}$$

where $\pm$ on the second line corresponds to the light rays moving counterclockwise (+) or clockwise (−) along the φ direction. The impact parameter b is defined as $|L|/E$, where L and E are the conserved angular momentum and energy of the photons, respectively. Note that we use a redefined affine parameter $\lambda \to \lambda/|L|$ in Eq. (6). From the last equation of Eq. (6), one can define the effective potential of light rays as

$$V_{\text{eff}}(r) = \frac{e^{-2\delta(r)}N(r)}{r^2}. \tag{7}$$

Particularly, an unstable photon sphere (or equivalently, a circular and unstable null geodesic) is determined by

$$V_{\text{eff}}(r_{\text{ph}}) = \frac{1}{b^2_{\text{ph}}}, \quad V'_{\text{eff}}(r_{\text{ph}}) = 0, \quad V''_{\text{eff}}(r_{\text{ph}}) < 0, \tag{8}$$

where r_{ph} is the radius of the photon sphere and b_{ph} is the corresponding impact parameter. In this paper, we focus on unstable photon spheres since they play an important role in determining the accretion disk image seen by a distant observer. For convenience, photon spheres are referred to as unstable photon spheres in the remainder of this paper unless we make an explicit statement to the contrary.

In this paper, we consider the HBH to be surrounded by a static and geometrically thin accretion disk, which is assumed to radiate isotropically in the rest frame of the matter. In addition, we take the disk emission to be optically thin by neglecting the absorption effect. Note that there exists compelling evidence indicating that an optically thin hot accretion flow may surround M87* or Sgr A* [123,124]. Moreover, the inclination angle between the line of sight to the observer and the accretion disk axis is presumed to be small (around 17°) in the observation of M87* [1]. Therefore, in this paper, we consider a simplified scenario with accretion disks being viewed from a face-on orientation, which is widely adopted and investigated in the literature [70–77]. To obtain the accretion disk image perceived by a distant observer, we evolve light rays from the observer's position backward in time. Furthermore, one can use m, the times that a certain ray intersects with the disk plane outside the horizon, to distinguish light rays' behavior. Following the definitions in [72], light rays with $m \leq 1$, $m = 2$, and $m \geq 3$ constitute the direct emission, the lensing ring, and the photon ring, respectively. Note that for a face-on accretion disk surrounding a black hole, the definition of m as the times of intersection with the disk is identical to that as the number of half orbits around the black hole. The observed total intensity $F_o(b)$ generated by a light ray of impact parameter b is a sum of the intensities from each intersection with the disk plane outside the horizon,

$$\begin{aligned}F_o(b) &= \int_{\nu_o} d\nu_o I_{\nu_o}(b) = \sum_m \int_{\nu_e} g(r) d\nu_e g^3(r) I_{\nu_e}(r)\Big|_{r=r_m(b)}\\ &= \sum_m g^4(r) F_e(r)\Big|_{r=r_m(b)},\end{aligned} \tag{9}$$

where $g(r)$ is the redshift factor, I_{ν_e} is the specific intensity at the emission frequency ν_e, I_{ν_o} is the specific intensity at the observed frequency ν_o, and $F_e = \int_{\nu_e} I_{\nu_e} d\nu_e$ is the total emitted intensity. Here, we have applied the $I_{\nu_o} = g^3(r) I_{\nu_e}$ by Liouville's theorem in the second equality. The function $r_m(b)$ $(m = 1, 2, 3\ldots)$, dubbed the transfer function, is the radial coordinate of the light ray crossing the disk plane at the mth time. Moreover, the slope of the transfer function, dr_m/db, is the demagnification factor of the mth image of the accretion disk. For simplicity, we set the total emitted intensity $F_e(r) = 1/r^2$ with $r > r_h$, which suffices to illustrate the major features of the accretion disk image. In this case, the observed total intensity is given by

$$F_o(b) = \sum_m \frac{N^2(r)e^{-4\delta(r)}}{r^2}\Big|_{r=r_m(b)}, \tag{10}$$

where we use $g(r) = \sqrt{N(r)}e^{-\delta(r)}$ [95]. When viewed in a face-on orientation, the 2D image of the accretion disk is

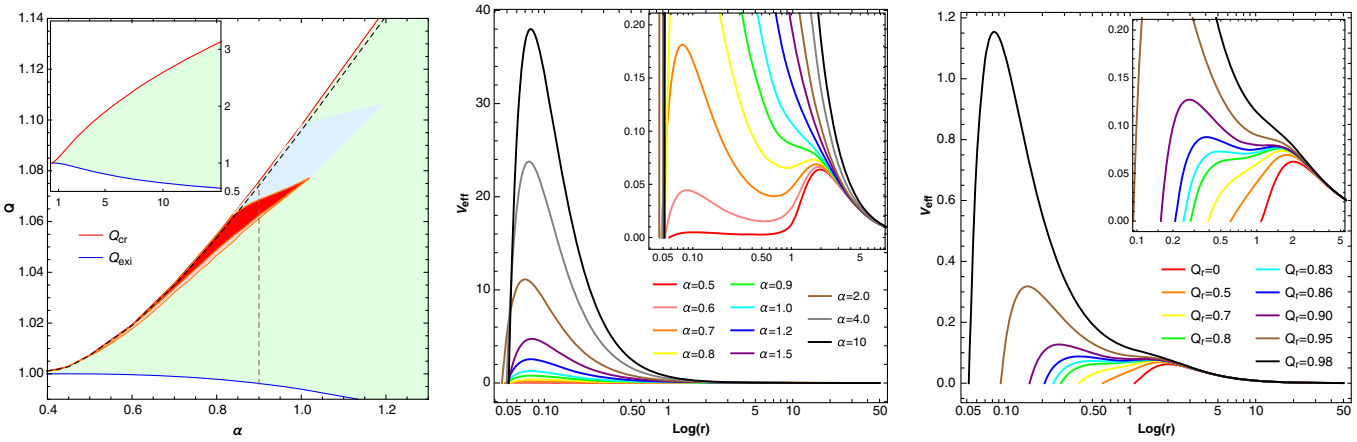

FIG. 1. Left panel: regions of four different HBH families in the Q-α plane—single-peak I (green), single-peak II (blue), double-peak I (orange), and double-peak II (red). The domain of the HBH solutions is bounded by the existence line (blue) and the critical line (red). The black dashed line and the vertical dashed line denote $Q_r \equiv (Q - Q_{\rm exi})/(Q_{\rm cr} - Q_{\rm exi}) = 0.98$ and $\alpha = 0.9$, respectively. The inset displays the domain of HBH solutions with a larger range of α, and shows that the single-peak I family occupies almost the whole HBH existence regime. Middle panel: profiles of the effective potentials at fixed $Q_r = 0.98$ for different α. The inset illustrates the change of the potential profiles, indicating a single-peak I → double-peak I → double-peak II → single-peak II → single-peak I transition with increasing α. Right panel: profiles of the effective potentials at fixed $\alpha = 0.9$ for different Q_r. The change of the potential profiles is zoomed in the inset, which presents a single-peak I → double-peak I → double-peak II → single-peak II transition as Q_r increases.

circularly symmetric. Taking account of the geometric interpretation of b, we can depict the 2D face-on image by employing $F_o(b) = F_o(\sqrt{X^2 + Y^2})$, where the coordinates (X, Y) span the observer's celestial plane.

III. NUMERICAL RESULTS

In this section, we present the numerical results about the optical appearance of the accretion disk surrounding the HBH black hole, viewed face-on. In the left panel of Fig. 1, we first display the domain of existence for HBH solutions to the action (1), which is bounded by the sets of existence and critical solutions, denoted by the $Q_{\rm exi}$ line (red line) and $Q_{\rm cr}$ line (blue line) in the $Q - \alpha$ plane, respectively. On the $Q_{\rm cr}$ line, the black hole horizon radius vanishes with the black hole mass and charge remaining finite. Furthermore, this domain can be divided into four parameter space regions, in one of which the effective potentials (7) have distinct profiles, e.g., the number of the maxima. In particular, we obtain four families of the HBH solutions.

(1) Single-peak I (green region): The potential has a single maximum, which is similar to Schwarzschild and RN black holes [69,125], for instance, the $\alpha = 10$ case (black line) in the middle panel of Fig. 1.
(2) Single-peak II (blue region): The potential has a single maximum and an "anklelike" structure, e.g., the $\alpha = 0.9$ case (green line) in the middle panel. The anklelike structure is characterized by a flattening of the potential, and corresponds to a transition between convexity and concavity of the effective potential. More precisely, its presence can be determined by the appearance of $V''_{\rm eff}(r) > 0$ in the region where $V'_{\rm eff}(r) < 0$.
(3) Double-peak I (orange region): The potential has two maxima at two different radii, and the peak of the potential at the smaller radius is lower than that at the larger radius, e.g., the $\alpha = 0.6$ case (pink line) in the middle panel.
(4) Double-peak II (red region): The potential has two maxima at two different radii, and the peak of the potential at the smaller radius is higher than that at the larger radius, e.g., the $\alpha = 0.7$ case (orange line) in the middle panel.

It can be observed from the inset in the left panel of Fig. 1 that the single-peak I family occupies almost the whole HBH existence regime, whereas the other three families only exist in a small α region near the $Q_{\rm cr}$ line.

To illustrate how the potential profile changes among different families, we display a set of potentials along the lines with fixed $Q_r \equiv (Q - Q_{\rm exi})/(Q_{\rm cr} - Q_{\rm exi}) = 0.98$ and fixed $\alpha = 0.9$ in the middle and right panels of Fig. 1, respectively. In the inset of the middle (right) panel, the profiles of the potentials with different α (Q_r) are zoomed in to better show how the potential profiles change with α (Q_r). As α increases with $Q_r = 0.98$, the middle panel (specifically, the inset therein) shows that the potential first has a single peak, then another peak at a smaller radius appears and grows, meanwhile the peak at the larger radius shrinks until it disappears, indicating the single-peak I → double-peak I → double-peak II → single-peak II → single-peak I transition. When Q_r increases with fixed $\alpha = 0.9$, the right panel and the inset therein present the single-peak I → double-peak I → double-peak II → single-peak II transition. In what follows, we display several representative cases to show the main features of each family. Note that the HBH mass M

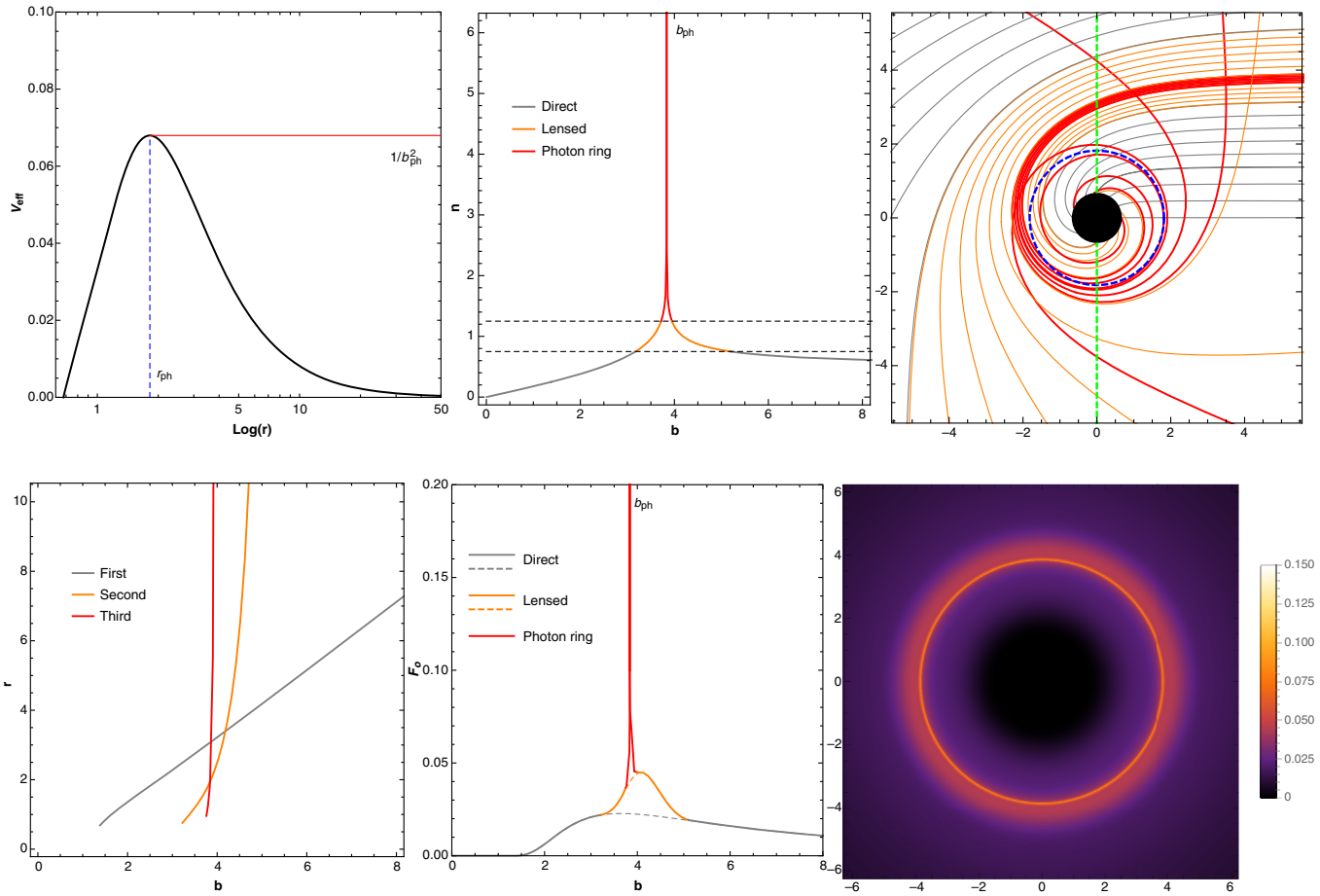

FIG. 2. Behavior of photons in a HBH with $\alpha = 0.9$ and $Q = 1.03$, which is in the single-peak I family, and the observational appearance of an optically and geometrically thin accretion disk around the HBH, viewed from a face-on orientation. Upper-left panel: profile of the effective potential, which possesses a single maximum. Upper-middle panel: total number of orbits $n = \Phi/(2\pi)$, where $\Phi = \Delta\varphi$ is the total change of the azimuthal angle outside the event horizon. The direct emission, the lensing ring, and the photon ring correspond to $n < 0.75$ (gray), $0.75 \leq n < 1.25$ (orange), and $n \geq 1.25$ (red), respectively. Upper-right panel: selection of photon trajectories within the direct, lensed, and photon ring bands. The blue dashed circle is the photon sphere, and the green line denotes the cross section of the disk plane. Lower-left panel: first three transfer functions $r_m(b)$ with $m = 1$ (gray), $m = 2$ (orange), and $m = 3$ (red), representing the radial coordinates of the first, second, and third intersections with the accretion disk. Lower-middle panel: observed total intensity $F_o(b)$ and the net contributions to the total flux from the direct (gray), lensed (orange), and photon ring (red) bands. Lower-right panel: 2D image of the accretion disk viewed in the observer's sky. A bright and narrow ring appears at the location of the photon ring.

is set to 1 without loss of generality in the rest of this section.

Interestingly, apart from two unstable photon spheres, a stable photon sphere, corresponding to the minimum of the effective potential, is observed to exist outside the event horizon of a HBH in the double-peak I and II families (e.g., the valleys of $V_{\rm eff}$ in the $\alpha = 0.6$ and $\alpha = 0.7$ cases shown in the inset of the middle panel in Fig. 1). In fact, the appearance of the stable photon sphere outside the event horizon is expected from the topological theorem in [126]. In [97], a topological argument gives that horizonless ultracompact objects must have at least one stable photon sphere (or light ring for rotating ultracompact objects). Moreover, stable photon spheres have also been found in wormholes of the Morris-Thorne class [38,98] and on the horizons of extreme static black holes [127]. In particular, it was suggested in [128] that the existence of very long-lived modes localized near stable photon spheres might make spacetime unstable. In our work, the potential endowed with double-peak structure provides an interesting example that an asymptotically flat black hole can have a stable photon sphere outside the event horizon. Effects of stable photon spheres on the HBH stability are beyond the scope of this work, and hence we leave them to future studies.

A. Single-peak potential

For the single-peak I family, we consider a HBH with $\alpha = 0.9$ and $Q = 1.03$ in Fig. 2. The potential with one maximum indicates a single photon sphere with radius $r_{\rm ph}$

and the corresponding impact parameter $b_{\rm ph}$. To consider the accretion disk viewed from a face-on orientation, we assume that an observer is placed at the far right of the upper-right panel, corresponding to the "north pole direction," and the disk lies in the equatorial plane with respect to the observer's orientation (dashed green line in the upper-right panel). Tracing a light ray backward from the observer, the total orbit number n is related to the total disk-crossing times m as $n<0.5\rightarrow m=0$, $0.5\leq n<0.75\rightarrow m=1$, $0.75\leq n<1.25\rightarrow m=2$, and $n\geq 1.25\rightarrow m\geq 3$. By definition, $m\leq 1$, $m=2$, and $m\geq 3$ correspond to the direct emission, the lensing ring, and the photon ring, respectively [72]. In the upper-middle panel, we plot n as a function of b and depict the direct, lensing, and photon ring bands in gray, orange, and red, respectively.

To obtain the observed intensity, we first calculate the transfer functions $r_m(b)$ with $m=1,2,3,\ldots$. In the lower-left panel of Fig. 2, we depict the transfer functions for $m=1$, 2, and 3, which are associated with the direct, lensing, and photon ring bands, respectively. Since the average slope of $r_m(b)$ roughly reflects the demagnified level of the mth image of the disk plane, it shows that the secondary image is highly demagnified, and the tertiary image is extremely demagnified. Via Eq. (10), the observed intensity F_o as a function of b is shown in the lower-middle panel, which presents a narrow spikelike photon ring (red) and a broader bumplike lensing ring (orange) superimposed on the direct emission (gray). One can see that the direct emission makes the dominant contribution to the overall intensity flux, whereas the lensing (photon) ring makes modest (small) contributions. To present the 2D image of the accretion disk seen by a distant observer, we project $F_o(b)$ to the observer's celestial (X,Y) plane via $b^2=X^2+Y^2$. In the lower-right panel, the observational appearance of the photon ring is shown to be a thin bright ring of radius $b_{\rm ph}$, which suggests that the photon ring makes a very small contribution to the total flux. More precisely, one can obtain the total observed intensity flux F of the direct, lensing, and photon ring bands by the integral $F=\int_\Omega 2\pi b F_o(b)db$, where Ω denotes the b range of the corresponding band. Thus the percentage of the total flux from the direct emission, the lensing ring, and the photon ring corresponds to $F_{\rm Direct}/F_{\rm Total}$, $F_{\rm Lensing}/F_{\rm Total}$, and $F_{\rm Photon}/F_{\rm Total}$, respectively, where $F_{\rm Total}=F_{\rm Direct}+F_{\rm Lensing}+F_{\rm Photon}$. Employing these formulas, we find that the direct emission, the lensing ring, and the photon ring contribute 85.7%, 11.6%, and 2.7% of the total flux, respectively. In [72], it was estimated that, for a Schwarzschild black hole, the lensing ring and the photon ring contribute around 5% and 0.25% of the total flux, respectively. Compared with the Schwarzschild case, the contribution from the photon ring of a HBH in the single-peak I family constitutes a much larger percentage of the total flux. Although the photon ring of the HBH is washed out in the blurred image at the current EHT's resolution (the left panel of Fig. 8), its flux might provide a distinctive feature in a relatively high resolution image, which could be viable in next generation EHT observations [129]. Moreover, there exists a completely dark area with vanishing intensity inside the photon ring, which is determined by the $m=0$ band.

On the other hand, the photon ring can play a nontrivial role in the observational appearance of an accretion disk around a HBH in the single-peak II family. A HBH with $\alpha=0.9$ and $Q=1.074$ is considered in Fig. 3, the upper-left panel of which shows that the effective potential has an anklelike structure around $\log r\sim 1$. This distinctive feature results in more complicated behavior of null geodesics and the observational appearance of emission from an accretion disk. Indeed, due to the flattening of the anklelike structure, photons can revolve around the anklelike structure multiple times, and cross the disk plane more than twice. So the upper-middle panel displays that, in addition to the sharp peak determined by the photon sphere at $b=b_{\rm ph}$, the $n(b)$ curve also possesses a much broader peak of finite height at $b>b_{\rm ph}$, which significantly widens the photon ring band. Note that a similar phenomenon has been reported in a wormhole scenario [38]. Consequently, as shown in the lower-middle panel, the photon ring makes a noticeable contribution to the total intensity flux, comparable to that of the lensing ring. Therefore, the photon ring plays an important role in determining the observational appearance of the accretion disk, leading to the presence of a bright ring and a concentric bright annular region, which can be observed in the lower-right panel. While the bright ring at the smaller radius, corresponding to the photon sphere, is barely visible due to the sharpness of the peak of $F_o(b)$ at $b=b_{\rm ph}$, the wide bright annular region at the larger radius is quite noticeable and comprises multiple concentric thin bright rings with different luminosities. Interestingly, the second and third transfer functions both exist over a larger range of b than those in the single-peak I family (lower-left panels of Figs. 2 and 3), thus resulting in less demagnification for secondary and tertiary images in the single-peak II family.

B. Double-peak potential

The prominent character of a double-peak potential is the presence of two maxima at $r=r_{\rm ph1}$ and $r=r_{\rm ph2}$ with $r_{\rm ph1}<r_{\rm ph2}$, corresponding to two photon spheres of radii $r_{\rm ph1}$ and $r_{\rm ph2}$ outside the horizon, respectively. The associated maximum values of the potential are $1/b_{\rm ph1}^2$ and $1/b_{\rm ph2}^2$, where $b_{\rm ph1}$ and $b_{\rm ph2}$ are the impact parameters of the photon spheres (see the upper-left panels of Figs. 4 and 5). As mentioned before, there are two families of double-peak potentials according to the magnitudes of the two maximum values of the potentials. For the double-peak

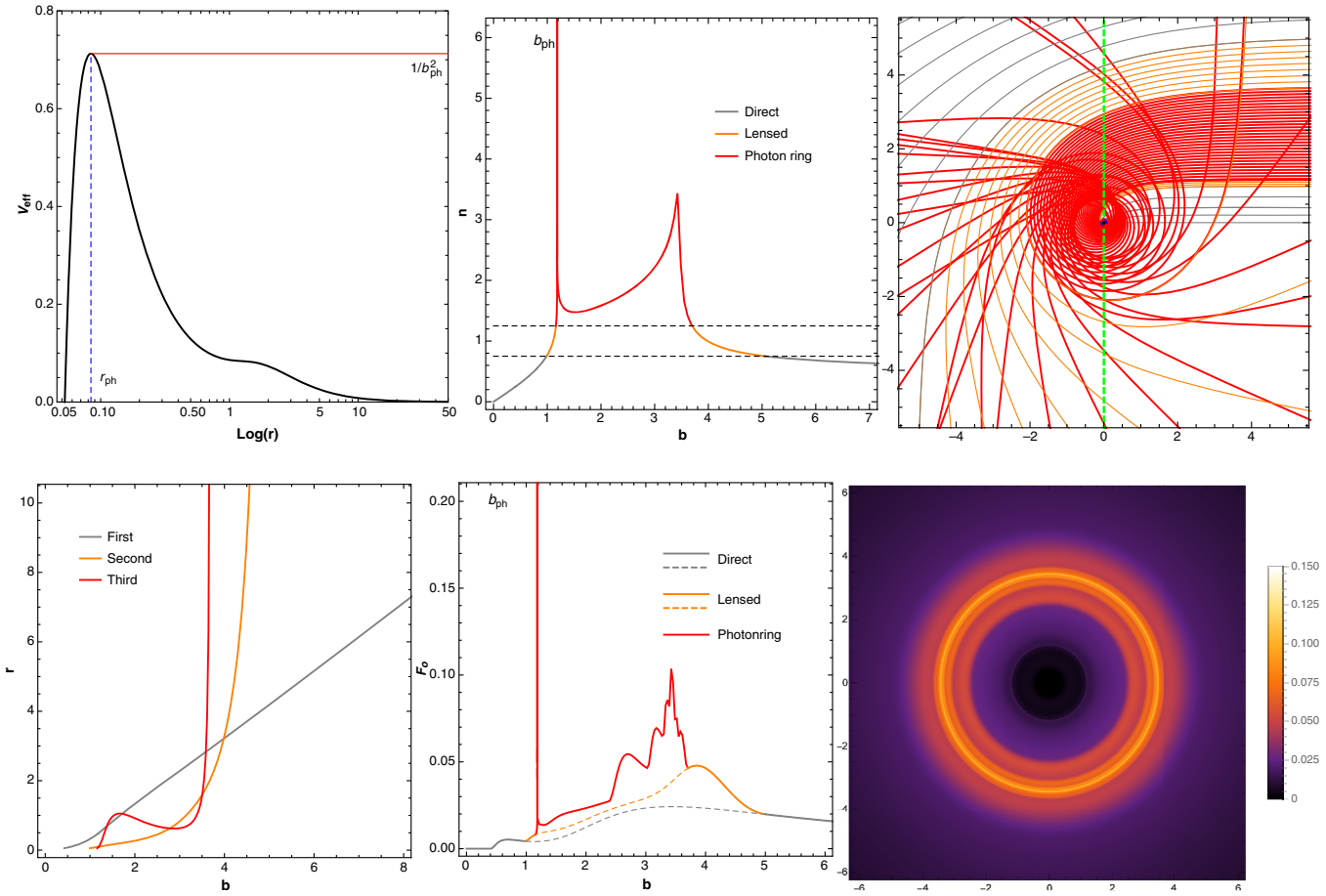

FIG. 3. Behavior of photons in a HBH with $\alpha = 0.9$ and $Q = 1.074$, which is in the single-peak II family, and the observational appearance of an optically and geometrically thin accretion disk around the HBH, viewed from a face-on orientation. The effective potential shows a flattening around $\log r \sim 1$ (upper-left panel), which leads to a finite broad peak in the $n - b$ plane (upper-middle panel). As a result, the width of the photon ring is significantly increased, and comparable to that of the lensing ring. Therefore, the photon ring can make a nontrivial net contribution to the observed flux $F_o(b)$ (lower-middle panel). Specifically, a bright and wide annulus, consisting of multiple concentric bright thin rings, appears outside the bright ring, corresponding to the photon sphere, in the accretion disk image (lower-right panel). Moreover, as indicated by the transfer functions, the secondary and tertiary images are less demagnified than those in the single-peak I family (lower-left panel).

I potential, the maximum at the smaller radius is lower than that at the larger radius (or equivalently, $b_{\rm ph1} > b_{\rm ph2}$). So the light rays revolving around the photon sphere of smaller radius cannot escape to infinity, rendering this photon sphere invisible to a distant observer. As a result, accretion disk images in the double-peak I family closely resemble those in the single-peak I family. On the other hand, both photon spheres can be responsible for obtaining the image of an accretion disk in the double-peak II family. In fact, two bright rings of arbitrarily large brightness, whose radii are $b_{\rm ph1}$ and $b_{\rm ph2}$, respectively, can appear in the image of the accretion disk. In what follows, we display two representative cases of the double-peak II family.

In Fig. 4, we consider a HBH with $\alpha = 0.9$ and $Q = 1.064$, for which the difference between $b_{\rm ph1}$ and $b_{\rm ph2}$ is small. As expected, the existence of two photon spheres endows both $n(b)$ and $F_o(b)$ curves with two infinite peaks at radii $b_{\rm ph1}$ and $b_{\rm ph2}$. As shown in the upper-middle panel, this two-peak structure extends the width of the photon ring band compared to the single-peak I case. It is observed in the lower-middle panel that the photon ring can make a non-negligible contribution to the observed intensity, which is comparable to that of the lensing ring. Moreover, the photon ring leads to some internal structure between the two peaks for the observed intensity. However, since the photon ring is not wide enough, the lower-right panel shows that the internal structure can hardly been seen in the 2D image, and the observational appearance of the photon ring is almost indistinguishable from that of a thin bright ring.

In Fig. 5, we consider another HBH with $\alpha = 0.9$ and $Q = 1.07$, for which the difference between $b_{\rm ph1}$ and $b_{\rm ph2}$ is large. As shown in the upper-left panel, the two

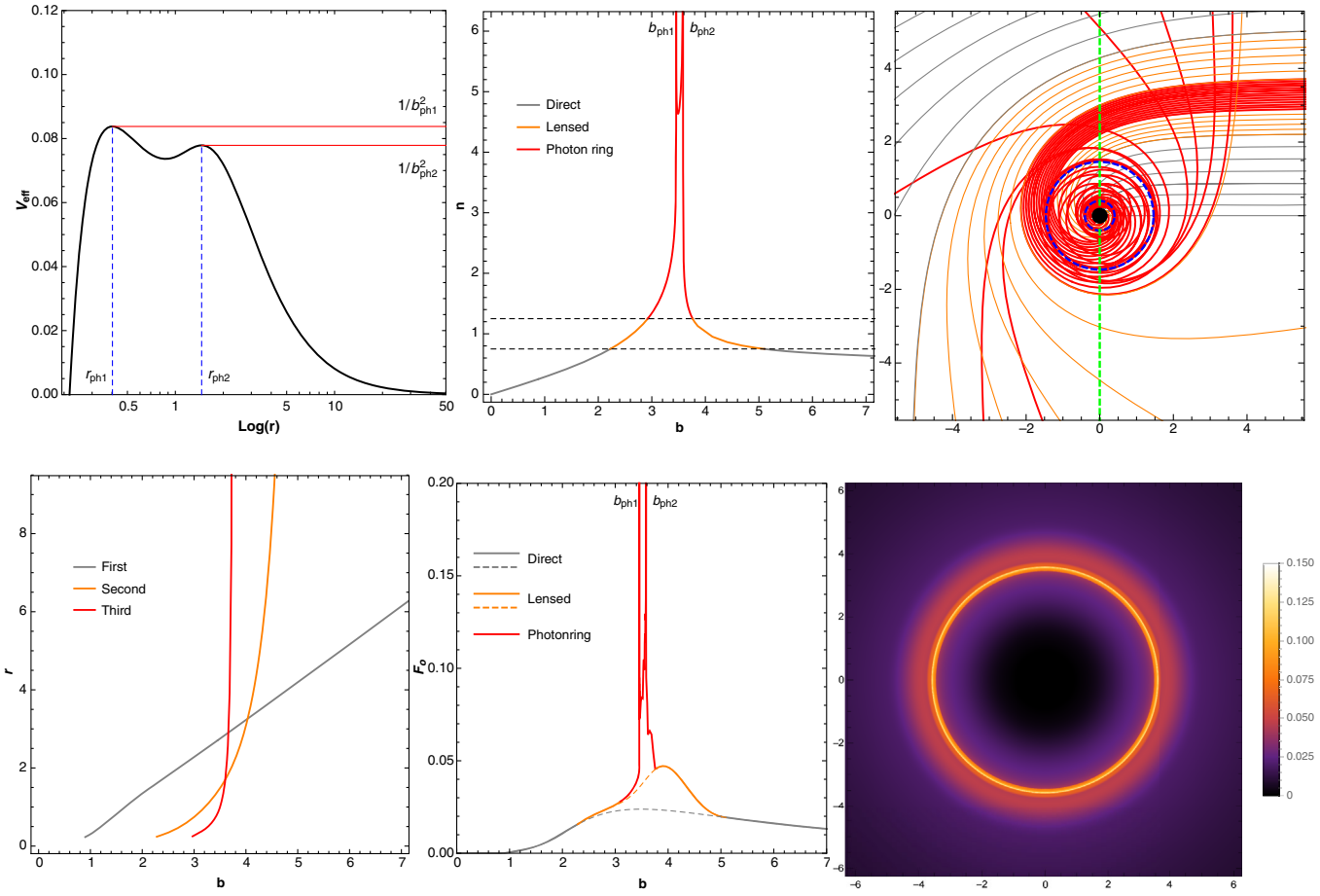

FIG. 4. Behavior of photons in a HBH with $\alpha = 0.9$ and $Q = 1.064$, which is in the double-peak II family, and the observational appearance of an optically and geometrically thin accretion disk around the HBH, viewed from a face-on orientation. The upper-left panel shows that the effective potential has two peaks of similar heights at $r = r_{\rm ph1}$ and $r = r_{\rm ph1}$, respectively. These two peaks correspond to two photon spheres (blue dashed circles), leading to two infinite peaks in $n(b)$ and $F_o(b)$ curves and a narrow photon ring (upper-middle and lower-middle panels). Due to the two photon spheres, the contribution from the photon ring to the observed flux $F_o(b)$ is comparable to that of the lensing ring, and hence is non-negligible (lower-middle panel). However, the internal structure of the photon ring is hardly visible in the accretion disk image because of the narrowness of the photon ring (lower-right panel).

maximum values of the effective potential are quite different, thus leading to a remarkably wider photon ring. The lower-middle panel exhibits that the lensing and photon rings both contribute appreciably to the total observed intensity, and the photon ring is notably wider than that in Fig. 4. In the lower-right panel, the 2D observed image is shown to have a bright thin ring at $b = b_{\rm ph1}$ and a bright annulus around $b = b_{\rm ph2}$, which consists of a bright ring at $b = b_{\rm ph2}$ and multiple concentric bright rings with different luminosity. In other words, the inner structure of the photon ring can be seen in the observed image since the photon ring is wide enough. The lower-left panels in Figs. 4 and 5 show that the secondary and tertiary images in Fig. 5 are less demagnified than those in Fig. 4. It is noteworthy that the anklelike structure of the potential in Fig. 3 is reminiscent of the maximum of the potential at $r = r_{\rm ph2}$ in Fig. 5.

C. Dependence on black hole charge and scalar coupling

Here, we turn to investigate the dependence of the size of the photon ring and shadow on the HBH charge Q and the scalar coupling α. To study the dependence on Q, we consider two cases with fixed $\alpha = 0.9$ and 10 in the upper and lower rows of Fig. 6, respectively. Note that the allowed parameter regions are bounded by the $Q_{\rm exi}$ line and/or the $Q_{\rm cr}$ line, which are shown in Fig. 1. The upper-left panel of Fig. 6 displays that, when $\alpha = 0.9$, the HBHs belong to the single-peak I (region on the left of the orange region), single-peak II (region on the right of the red region), double-peak I (orange region), or double-peak II (red region) families, depending on the value of the HBH charge. From the upper-middle panel, one can see that the photon ring (red region) of the HBHs in the single-peak II and double-peak II families are quite wide, thus indicating that the photon rings can play a relevant role in

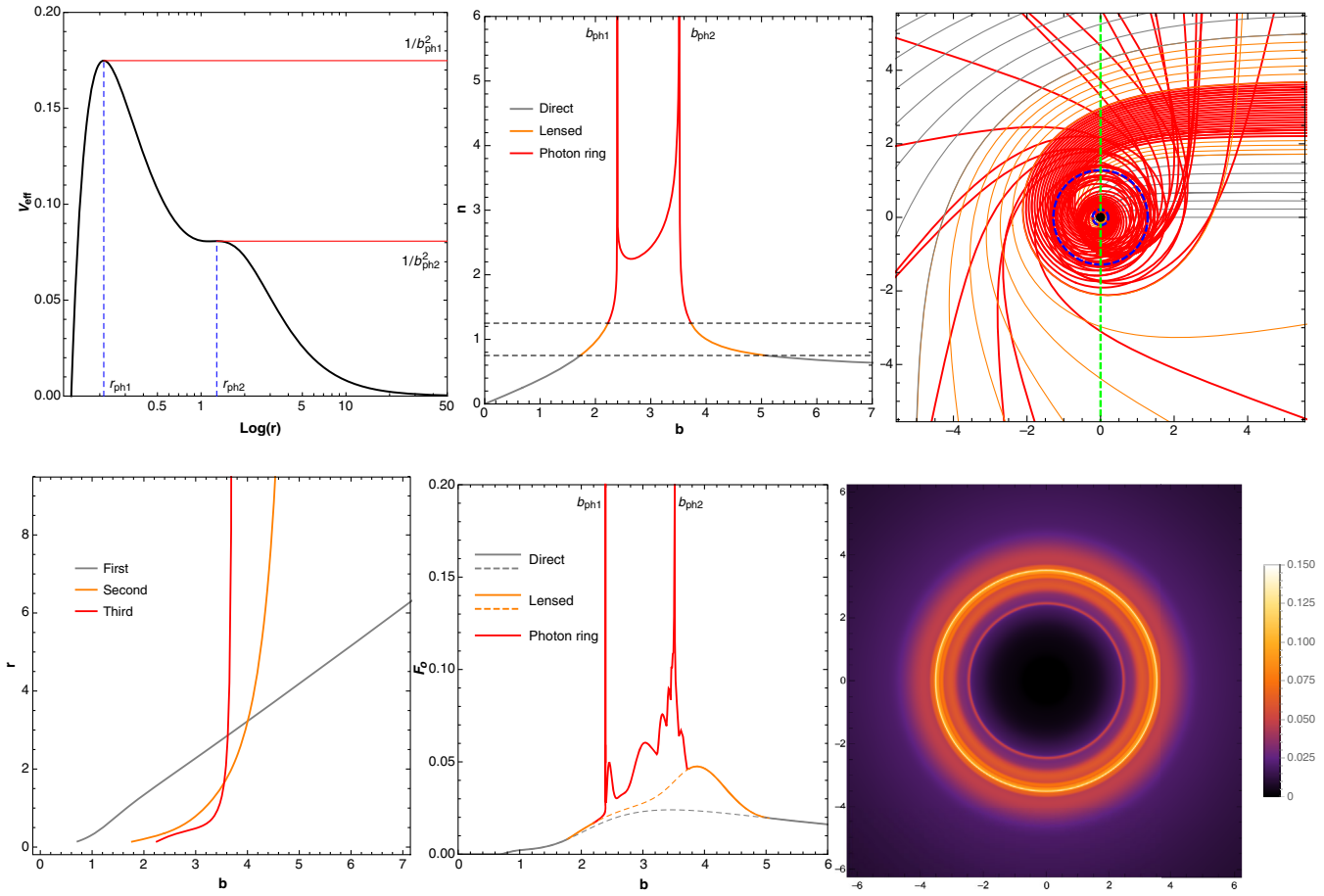

FIG. 5. Behavior of photons in a HBH with $\alpha = 0.9$ and $Q = 1.07$, which is in the double-peak II family, and the observational appearance of an optically and geometrically thin accretion disk around the HBH, viewed from a face-on orientation. Compared to Fig. 4, the photon ring here becomes significantly wider (upper-middle and lower-middle panels) since the two maximum values of the effective potential are well separated (upper-left panel). Therefore, the photon ring can make a sizable contribution to the total flux (lower-middle panel), and the internal structure of the photon ring, which is made up of multiple concentric bright rings, can be observed in the 2D image (lower-right panel).

determining the observed accretion disk images. Moreover, as the HBH charge increases toward the $Q_{\rm cr}$ line, the width of the photon ring grows until the photon ring splits into a narrow photon ring of smaller radius and a broad one of larger radius in the image plane. While the photon ring of smaller radius is barely visible in the observed 2D image, the one of larger radius can make a non-negligible contribution to the total intensity and the accretion disk image. Therefore, it is expected that the accretion disk image in the two photon rings scenario is quite similar to those shown in Figs. 3 and 5. On the other hand, the HBH with $\alpha = 10$ is always in the single-peak I family, which is shown in the inset of the left panel of Fig. 1. In this case, the lower-middle panel of Fig. 6 displays that the photon ring is always very narrow, and the lensing (orange and red regions) and photon rings decrease in size with Q increasing toward $Q_{\rm cr}$. Around $Q = Q_{\rm cr}$, the lensing ring also becomes very narrow, and makes a negligible contribution to the observed intensity.

In this paper, the term "standard shadow" is used to refer to the area inside the (smaller) photon sphere (i.e., the apparent boundary [10,11]). Specifically, the radius of the standard shadow is the impact parameter of the smaller photon sphere if there exist two photon spheres [95]. From the left column of Fig. 6, it is observed that the standard shadow of a HBH in the $\alpha = 0.9$ and 10 cases shrinks with increasing Q and vanishes at $Q = Q_{\rm cr}$, where the HBH horizon becomes zero. For $\alpha = 0.9$, the standard shadow radius decreases at a larger decreasing rate in the single-peak II and double-peak II families. In the middle column of Fig. 6, the black regions denote the completely dark area with vanishing intensity, and are also shown to decrease in size with increasing Q and vanish at $Q = Q_{\rm cr}$. For comparison, we also plot the impact parameters of the photon spheres of RNBHs with $M = 1$ in the right column of Fig. 6. In the coexisting Q range of the RNBH and HBH, one can see that the standard shadow of the RNBH is larger than that of the HBH in the $\alpha = 0.9$ case (upper-right panel

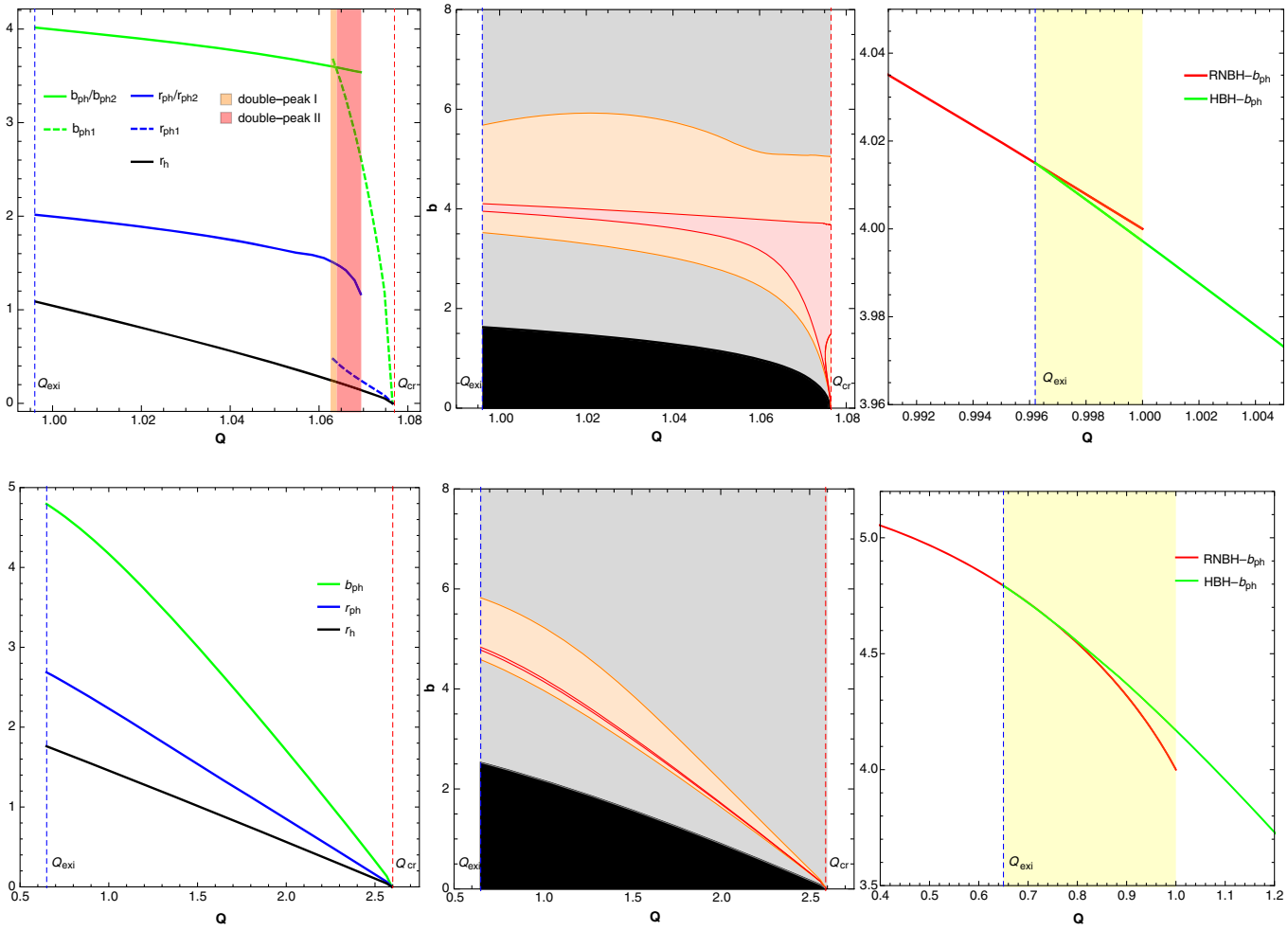

FIG. 6. Dependence of quantities of interest on the black hole charge Q for HBHs with $\alpha = 0.9$ (upper row) and $\alpha = 10$ (lower row). Left panels: photon sphere radii, $r_{\rm ph}$, $r_{\rm ph1}$, and $r_{\rm ph2}$, the associated impact parameters, $b_{\rm ph}$, $b_{\rm ph1}$, and $b_{\rm ph1}$, and the horizon radius r_h as functions of Q. As shown in Fig. 1, the range of Q is bounded by the existence charge $Q_{\rm exi}$ (black dashed line) and critical charge $Q_{\rm cr}$ (red dashed line). With increasing Q from $Q_{\rm exi}$, the HBH with $\alpha = 0.9$ undergoes the single-peak I (region between the $Q_{\rm exi}$ line and the orange region), double-peak I (orange region), double-peak II (red region), and the single-peak II (region between the red region and the $Q_{\rm cr}$ line) families, while the HBH with $\alpha = 10$ remains in the single-peak I family. The impact parameter of the (smaller) photon sphere is identified as the radius of the HBH standard shadow, which decreases in size as Q increases, and disappears at $Q = Q_{\rm cr}$. Middle panels: ranges of the direct emission (black, gray, orange, and red regions), the lensing ring (orange and red regions), and the photon ring (red region) as functions of Q. The black region denotes the $m = 0$ band, corresponding to the completely dark region. When $\alpha = 0.9$, the range of the photon ring can be quite noticeable for large enough Q (e.g., in the single-peak II and double-peak II families), thus indicating that the photon ring contributes nontrivially to the observed flux. When $\alpha = 10$, the photon ring always has a very narrow range, and hence makes a negligible contribution to the flux. Right panels: impact parameters of the RNBH (red) and HBH (green) versus Q in the coexistence region (yellow region). For a given Q, the HBH (RNBH) has a smaller standard shadow for $\alpha = 0.9$ ($\alpha = 10$).

of Fig. 6), and vice versa in the $\alpha = 10$ case (lower-right panel of Fig. 6), which is consistent with the result in [91].

In Fig. 7, three cases with fixed $Q = 0.8$ (left column), $Q = 1.06$ (middle column), and $Q = 2$ (right column) are presented to study the dependence on the scalar coupling α. As shown in the upper row, the size of the standard shadow becomes larger for a stronger scalar coupling in all cases. For $Q = 0.8$, the ranges of the photon and lensing rings are fairly insensitive to α. In the near $Q_{\rm cr}$-line regime, HBHs with $Q = 1.06$ are in the double-peak II family, and the photon ring's contribution to the observed intensity cannot be neglected. On the other hand, the ranges of the photon and lensing rings of HBHs with $Q = 2$ become zero at the $Q_{\rm cr}$ line. Finally, it is interesting to note that the stronger the α, the larger the completely dark area becomes.

D. Blurred accretion disk images

So far, we have considered high resolution images of HBHs surrounded by an accretion disk, which present

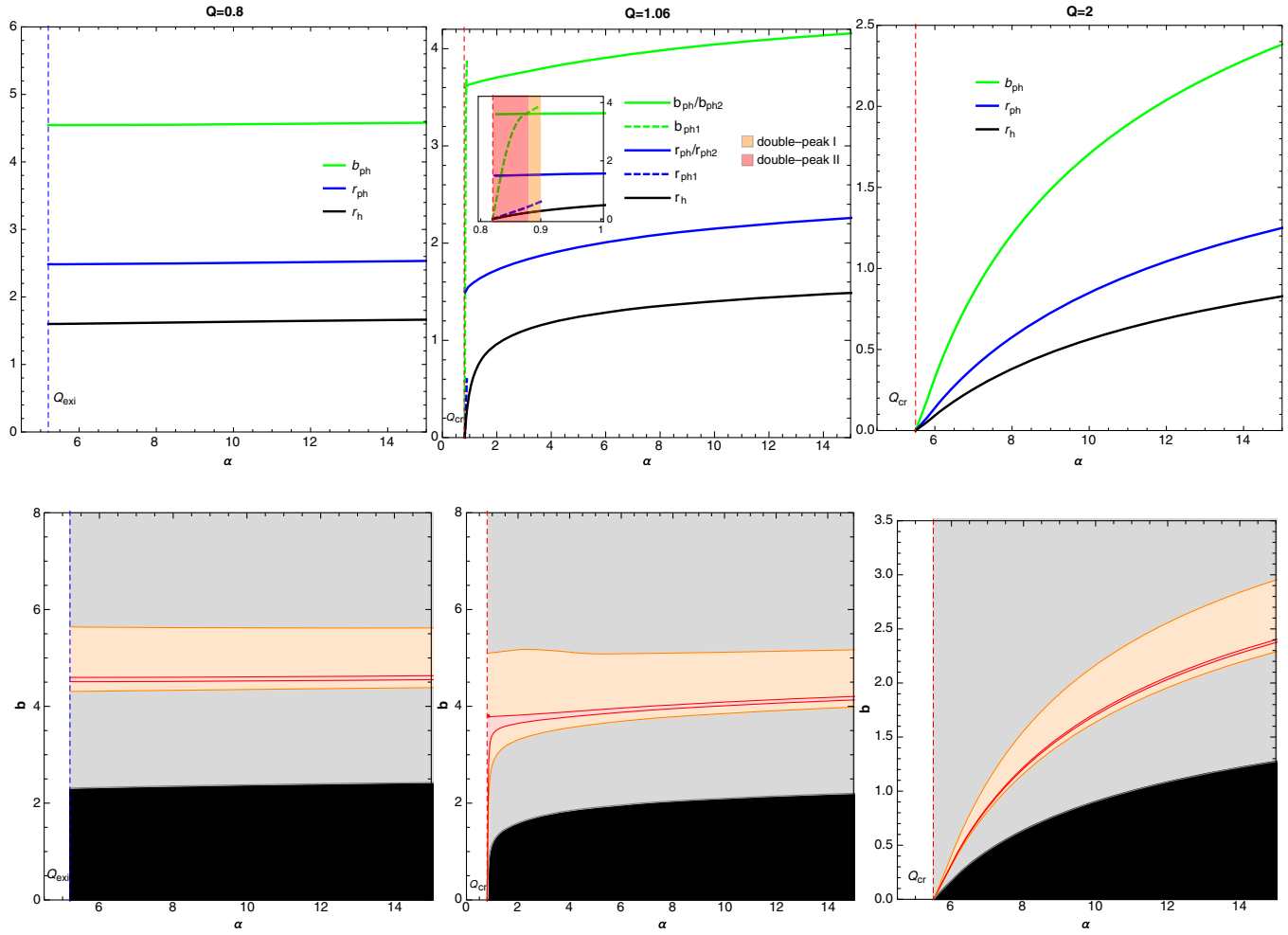

FIG. 7. Dependence of quantities of interest on the scalar coupling α for HBHs with $Q = 0.8$ (left panels), $Q = 1.06$ (middle panels), and $Q = 2$ (right panels). For the $Q = 0.8$ and $Q = 2$ cases, the HBHs are always in the single-peak I family. As α increases, the HBH with $Q = 1.06$ belongs to the double-peak II, double-peak I, and single-peak I families, respectively. The allowed range of α is bounded from below by the $Q_{\rm exi}$ line in the $Q = 0.8$ case, and by the $Q_{\rm cr}$ line in the $Q = 1.06$ and $Q = 2$ cases. Upper row: event horizon radii (black), the photon sphere radii (blue), and the corresponding impact parameters (green) versus α. The standard shadow grows as α increases. Lower row: ranges of the direct emission (black, gray, orange, and red regions), the lensing ring (orange and red regions), and the photon ring (red region) as functions of α. The black region denotes the completely dark region. The photon ring can play a relevant role for a HBH with $Q = 1.06$, that is, close enough to the $Q_{\rm cr}$ line.

some interesting features of the photon ring. To gain some insight into the effects of the photon ring on a realistic observation, we blur the images of the accretion disk in Figs. 2–5 with a Gaussian filter with standard derivation equal to $1/12$ the field of view to mimic the EHT resolution [72], as shown in the lower row of Fig. 8. In Fig. 8, the white dotted circles represent critical circles, whose radii are the impact parameters of photon spheres, and the standard shadow is defined as the region inside the critical circle or that of smaller radius if there exist two photon spheres.

In the first column of Fig. 8, we display the high resolution and blurred images of the HBH from Fig. 2, which is in the single-peak I family. The blurred image is primarily determined by the direct emission and the lensing ring, and has a blurred bright ring at the location of the lensing ring, which indicates that the observed shadow almost coincides with the standard shadow. In the second column, we exhibit the high resolution and blurred images of the HBH of the double-peak II family from Fig. 4, which has two critical circles of similar radii. Compared with the single-peak I family, the existence of two photon spheres slightly increases the brightness of the blurred bright ring. In addition, the observed shadow in the blurred image is almost the same as the standard shadow.

On the other hand, when the photon ring is wide enough (e.g., Figs. 3 and 5), its effects can become quite noticeable in the blurred images. Indeed, the high resolution and blurred images of the HBH of the double-peak II family from Fig. 5 are shown in the third column of Fig. 8. In this

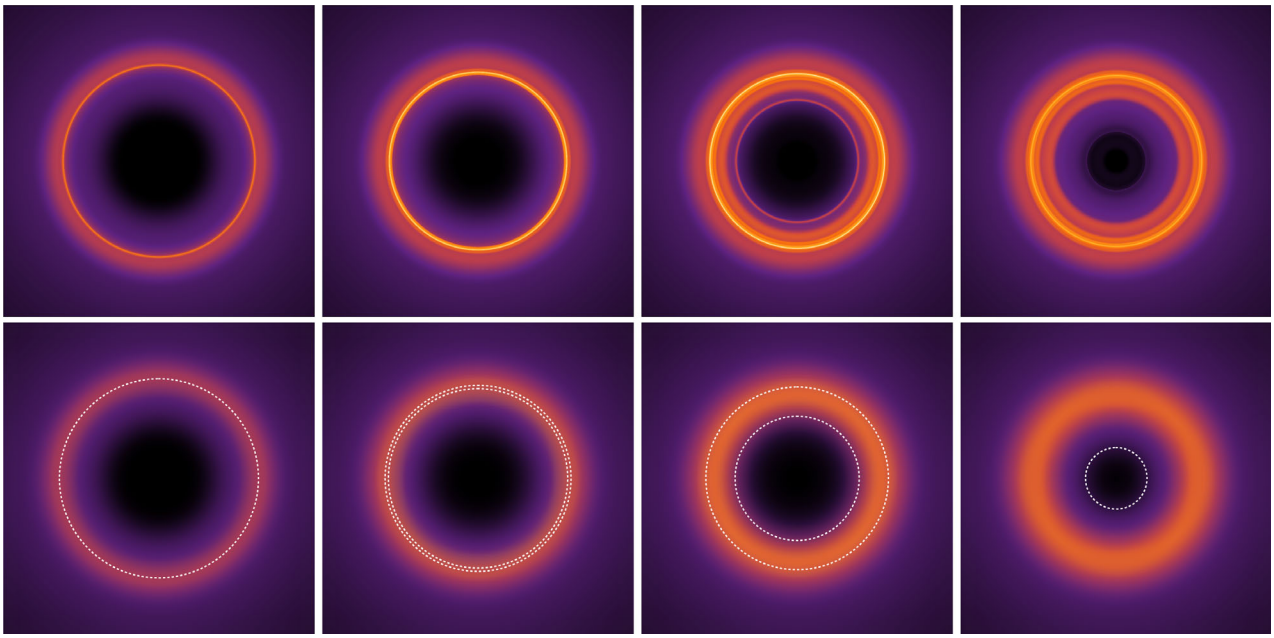

FIG. 8. High resolution and blurred images of the HBHs from Fig. 2 (first column, the single-peak I solution with $Q = 1.03$), Fig. 4 (second column, the double-peak II solution with $Q = 1.064$), Fig. 5 (third column, the double-peak II solution with $Q = 1.07$), and Fig. 3 (last column, the single-peak II solution with $Q = 1.074$). The high resolution images are blurred to correspond roughly to the EHT resolution. The white dotted circles denote critical circles associated with photon spheres, and the (smaller) critical circle is identified as the boundary of the standard shadow, which shrinks in size with increasing Q. For the HBHs with $Q = 1.07$ and 1.074, the photon ring is wide enough to leave imprints on the blurred images, where brighter and wider blurred rings are observed.

case, the radii of the two critical circles are quite different, which significantly increases the width of the photon ring. Although the internal structure of the photon ring is washed out by the blurring, the wide photon ring leads to a brighter and wider blurred ring than in the single-peak I family. Since the inner edge of the blurred bright ring is at the smaller critical circle, the observed shadow nearly matches the standard shadow. In the last column, the high resolution and blurred images of the HBH of the single-peak II family from Fig. 2 are presented. The anklelike structure of the effective potential also notably increases the brightness and width of the blurred bright ring. Moreover, the blurred bright ring is at the location of the anklelike structure, and hence has a large radius than the critical circle, which means that the observed shadow is larger than the standard shadow.

IV. CONCLUSION

In this paper, we investigated the behavior of null geodesics and observational appearance of a HBH surrounded by an optically and geometrically thin accretion disk in the EMS model with an exponential scalar coupling. Depending on the profile of the effective potentials for photons, we found that the HBH solutions are categorized into four different families, namely, single-peak I, single-peak II, double-peak I, and double-peak II. The single-peak I family dominates the allowed parameter space, while the other three families exist in a small region with small α and large Q. For the single-peak I solution, the photon ring is very narrow and makes little contribution to the total brightness. Therefore, the accretion disk images bear much similarity to those of various static black holes with a single-peak potential [65,72,74,75], e.g., a bright ring due to the lensing ring shows up (Fig. 2). On the other hand, an additional ankle- or peaklike structure emerges in the single-peak II and double-peak II solutions, and results in the appearance of a new finite or infinite peak in the $n(b)$ curve. Consequently, the photon ring can become sufficiently broader, and its inner structure comes into play, resulting in two bright annuluses in the observed image (Figs. 3 and 5). The annulus of smaller radius is quite narrow, while the one of larger radius is much wider, comprising multiple concentric thin bright rings with different luminosities. To illustrate the effects of the photon ring on observations, we presented the images of the HBHs at low resolutions, roughly corresponding to the EHT resolution (Fig. 8). For the single-peak II and double-peak II solutions, the details of bright annuluses are washed out, giving a considerably bright and wide ring in the blurred image.

We end with some comments on future studies from several perspectives. In this paper, we considered the concept of a "photon ring," which is defined as the collection of all $m \geq 3$ bands [72]. Since we observed the complicated inner structure inside the wide photon ring

(Figs. 3 and 5), it would be interesting to study this rich structure by performing a detailed analysis on each $m \geq 3$ band. Moreover, the ankle- and peaklike structures in the effective potentials in the aforementioned two cases behave like plateaus (upper-left panels of Figs. 3 and 5), which is reminiscent of the potential profiles reported in [130,131]. This suggests that a marginally unstable photon sphere is likely to appear during the transition between the single-peak II and double-peak II families. In addition, apart from the exponential coupling of the EMS model considered in this paper, exploring other coupling functions may provide us with more novel phenomena about the photon spheres and disk images. Finally, it would gain more insight into the modified gravity by considering a rotating HBH surrounded by an accretion disk and comparing it with black hole images released in future observations, such as the Next Generation Very Large Array [132], the Thirty Meter Telescope [133], and the BlackHoleCam [134].

ACKNOWLEDGMENTS

We thank Guangzhou Guo and Li Li for their helpful discussions and suggestions. This work is supported in part by NSFC (Grants No. 11875196, No. 11375121, No. 11947225, and No. 11005016).

APPENDIX: LIGHT PROPAGATION IN THE EMS MODEL

In this appendix, we use the geometric-optics approximation [135–137] to derive the equations of geometric optics governing light propagation in the EMS model with the action

$$S = \int d^4x\sqrt{-g}[\mathcal{R} - 2\partial_\mu\phi\partial^\mu\phi - e^{\alpha\phi^2}F_{\mu\nu}F^{\mu\nu}]. \tag{A1}$$

The equation of motion for the electromagnetic field A^μ is then given by

$$\partial_\mu[\sqrt{-g}e^{\alpha\phi^2}F^{\mu\nu}] = 0. \tag{A2}$$

Assuming the wavelength of the photon is much smaller than the physical scales of the metric and scalar fields (i.e., in the geometric-optics limit), we consider the ansatz

$$A^\mu = \mathrm{Re}[\mathcal{A}^\mu \exp(i\psi/\epsilon)], \tag{A3}$$

where A^μ is the slowly evolving amplitude and ψ is a rapidly oscillating function of time and space. Here, we introduce a small parameter ϵ to keep track of various order of terms, and the geometric-optics limit corresponds to $\epsilon \ll 1$. The wave vector k_μ of the light rays is identified as

$$k_\mu \equiv \partial_\mu\psi, \tag{A4}$$

where k_μ satisfies $\nabla_\mu k_\nu = \nabla_\nu k_\mu$ since the rays travel in the direction normal to the electromagnetic wave front [135]. We choose to work in the Lorentz gauge $\nabla_\mu A^\mu = 0$, which leads to

$$\epsilon^0\nabla_\mu\mathcal{A}^\mu + i\epsilon^{-1}\mathcal{A}^\mu k_\mu = 0. \tag{A5}$$

In the geometric-optics limit, the terms of order ϵ^0 and ϵ^{-1} in Eq. (A5) both vanish, namely, $\nabla_\mu A^\mu = 0$ and $A^\mu k_\mu = 0$. Putting all the pieces together, one can rewrite the equation of motion (A2) as a sum of terms of order ϵ^0, ϵ^{-1}, and ϵ^{-2},

$$\begin{aligned}&\epsilon^0\{f'(\phi)\partial_\mu\phi(\nabla^\mu\mathcal{A}^\nu - \nabla^\nu\mathcal{A}^\mu) + f(\phi)(\nabla_\mu\nabla^\mu\mathcal{A}^\nu - \nabla_\mu\nabla^\nu\mathcal{A}^\mu)\}\\ &+ i\epsilon^{-1}\{f'(\phi)\partial_\mu\phi(\mathcal{A}^\nu k^\mu - \mathcal{A}^\mu k^\nu)\\ &+ f(\phi)(2k^\mu\nabla_\mu\mathcal{A}^\nu + \mathcal{A}^\nu\nabla_\mu k^\mu)\} - \epsilon^{-2}\{f(\phi)\mathcal{A}^\nu k^\mu k_\mu\} = 0.\end{aligned} \tag{A6}$$

Again, each term of different ϵ order in Eq. (A6) shall vanish individually in the geometric-optics limit. Due to the nontriviality of $f(\phi)$ and A_μ, the leading term of order ϵ^{-2} reduces to the null condition,

$$k^\mu k_\mu = 0. \tag{A7}$$

Acting on the above equation with a covariant derivative yields

$$k^\mu\nabla_\mu k_\nu = 0, \tag{A8}$$

where we have used $\nabla_\mu k_\nu = \nabla_\nu k_\mu$. Equation (A8) shows that light rays of the EMS model are described by null geodesics in the geometric-optics limit.

[1] K. Akiyama *et al.*, First M87 Event Horizon Telescope results. I. The shadow of the supermassive black hole, Astrophys. J. Lett. **875**, L1 (2019).

[2] K. Akiyama *et al.*, First M87 Event Horizon Telescope results. II. Array and instrumentation, Astrophys. J. Lett. **875**, L2 (2019).

[3] K. Akiyama *et al.*, First M87 Event Horizon Telescope results. III. Data processing and calibration, Astrophys. J. Lett. **875**, L3 (2019).
[4] K. Akiyama *et al.*, First M87 Event Horizon Telescope results. IV. Imaging the central supermassive black hole, Astrophys. J. Lett. **875**, L4 (2019).
[5] K. Akiyama *et al.*, First M87 Event Horizon Telescope results. V. Physical origin of the asymmetric ring, Astrophys. J. Lett. **875**, L5 (2019).
[6] K. Akiyama *et al.*, First M87 Event Horizon Telescope results. VI. The shadow and mass of the central black hole, Astrophys. J. Lett. **875**, L6 (2019).
[7] K. Akiyama *et al.*, First M87 Event Horizon Telescope results. VII. Polarization of the ring, Astrophys. J. Lett. **910**, L12 (2021).
[8] K. Akiyama *et al.*, First M87 Event Horizon Telescope results. VIII. Magnetic field structure near the event horizon, Astrophys. J. Lett. **910**, L13 (2021).
[9] J. L. Synge, The escape of photons from gravitationally intense stars, Mon. Not. R. Astron. Soc. **131**, 463 (1966).
[10] J. M. Bardeen, W. H. Press, and S. A. Teukolsky, Rotating black holes: Locally nonrotating frames, energy extraction, and scalar synchrotron radiation, Astrophys. J. **178**, 347 (1972).
[11] J. M. Bardeen, Timelike and null geodesics in the Kerr metric, in *Black Holes, Proceedings of the Les Houches Summer School, Session XXIII*, edited by C. DeWitt and B. S. DeWitt (Gordon and Breach, Science Publishers, One Park Avenue, New York, 1973).
[12] V. Bozza, Gravitational lensing by black holes, Gen. Relativ. Gravit. **42**, 2269 (2010).
[13] Z. Li and C. Bambi, Measuring the Kerr spin parameter of regular black holes from their shadow, J. Cosmol. Astropart. Phys. 01 (2014) 041.
[14] N. Tsukamoto, Zilong Li, and C. Bambi, Constraining the spin and the deformation parameters from the black hole shadow, J. Cosmol. Astropart. Phys. 06 (2014) 043.
[15] A. Abdujabbarov, M. Amir, B. Ahmedov, and S. G. Ghosh, Shadow of rotating regular black holes, Phys. Rev. D **93**, 104004 (2016).
[16] N. Tsukamoto, Black hole shadow in an asymptotically-flat, stationary, and axisymmetric spacetime: The Kerr-Newman and rotating regular black holes, Phys. Rev. D **97**, 064021 (2018).
[17] R. Kumar and S. G. Ghosh, Black hole parameter estimation from its shadow, Astrophys. J. **892**, 78 (2020).
[18] I. Dymnikova and K. Kraav, Identification of a regular black hole by its shadow, Universe **5**, 163 (2019).
[19] F. Atamurotov, S. G. Ghosh, and B. Ahmedov, Horizon structure of rotating Einstein-Born-Infeld black holes and shadow, Eur. Phys. J. C **76**, 273 (2016).
[20] Z. Stuchlík and J. Schee, Shadow of the regular Bardeen black holes and comparison of the motion of photons and neutrinos, Eur. Phys. J. C **79**, 44 (2019).
[21] T.-C. Ma, H.-X. Zhang, H.-R. Zhang, Y. Chen, and J.-B. Deng, Shadow cast by a rotating and nonlinear magnetic-charged black hole in perfect fluid dark matter, Mod. Phys. Lett. A **36**, 2150112 (2021).
[22] Z. Hu, Z. Zhong, P.-C. Li, M. Guo, and B. Chen, QED effect on a black hole shadow, Phys. Rev. D **103**, 044057 (2021).
[23] S. I. Kruglov, The shadow of M87* black hole within rational nonlinear electrodynamics, Mod. Phys. Lett. A **35**, 2050291 (2020).
[24] L. Ma and H. Lu, Bounds on photon spheres and shadows of charged black holes in Einstein-Gauss-Bonnet-Maxwell gravity, Phys. Lett. B **807**, 135535 (2020).
[25] S.-W. Wei and Y.-X. Liu, Testing the nature of Gauss-Bonnet gravity by four-dimensional rotating black hole shadow, Eur. Phys. J. Plus **136**, 436 (2021).
[26] X.-X. Zeng, H.-Q. Zhang, and H. Zhang, Shadows and photon spheres with spherical accretions in the four-dimensional Gauss-Bonnet black hole, Eur. Phys. J. C **80**, 872 (2020).
[27] M. Guo and P.-C. Li, Innermost stable circular orbit and shadow of the 4D Einstein-Gauss-Bonnet black hole, Eur. Phys. J. C **80**, 588 (2020).
[28] F. Bacchini, D. R. Mayerson, B. Ripperda, J. Davelaar, H. Olivares, T. Hertog, and B. Vercnocke, Fuzzball shadows: Emergent horizons from microstructure, arXiv:2103.12075.
[29] D. Ayzenberg and N. Yunes, Black hole shadow as a test of general relativity: Quadratic gravity, Classical Quantum Gravity **35**, 235002 (2018).
[30] L. Amarilla, E. F. Eiroa, and G. Giribet, Null geodesics and shadow of a rotating black hole in extended Chern-Simons modified gravity, Phys. Rev. D **81**, 124045 (2010).
[31] S. Dastan, R. Saffari, and S. Soroushfar, Shadow of a charged rotating black hole in $f(R)$ gravity, arXiv:1606.06994.
[32] A. Addazi, S. Capozziello, and S. Odintsov, Chaotic solutions and black hole shadow in $f(R)$ gravity, Phys. Lett. B **816**, 136257 (2021).
[33] L. Amarilla and E. F. Eiroa, Shadow of a rotating brane-world black hole, Phys. Rev. D **85**, 064019 (2012).
[34] M. Guo, S. Song, and H. Yan, Observational signature of a near-extremal Kerr-Sen black hole in the heterotic string theory, Phys. Rev. D **101**, 024055 (2020).
[35] R. Kumar, S. G. Ghosh, and A. Wang, Gravitational deflection of light and shadow cast by rotating Kalb-Ramond black holes, Phys. Rev. D **101**, 104001 (2020).
[36] T. Zhu, Q. Wu, M. Jamil, and K. Jusufi, Shadows and deflection angle of charged and slowly rotating black holes in Einstein-Æther theory, Phys. Rev. D **100**, 044055 (2019).
[37] P. V. P. Cunha and C. A. R. Herdeiro, Shadows and strong gravitational lensing: A brief review, Gen. Relativ. Gravit. **50**, 42 (2018).
[38] R. Shaikh, P. Banerjee, S. Paul, and T. Sarkar, A novel gravitational lensing feature by wormholes, Phys. Lett. B **789**, 270 (2019); Erratum, Phys. Lett. B **791**, 422 (2019).
[39] M. Wielgus, J. Horak, F. Vincent, and M. Abramowicz, Reflection-asymmetric wormholes and their double shadows, Phys. Rev. D **102**, 084044 (2020).
[40] J. Peng, M. Guo, and X.-H. Feng, Observational signature and additional photon rings of asymmetric thin-shell wormhole, arXiv:2102.05488.

[41] P. V. P. Cunha, J. A. Font, C. Herdeiro, E. Radu, N. Sanchis-Gual, and M. Zilhão, Lensing and dynamics of ultracompact bosonic stars, Phys. Rev. D **96**, 104040 (2017).
[42] H. Olivares, Z. Younsi, C. M. Fromm, M. De Laurentis, O. Porth, Y. Mizuno, H. Falcke, M. Kramer, and L. Rezzolla, How to tell an accreting boson star from a black hole, Mon. Not. R. Astron. Soc. **497**, 521 (2020).
[43] R. Shaikh, P. Kocherlakota, R. Narayan, and P. S. Joshi, Shadows of spherically symmetric black holes and naked singularities, Mon. Not. R. Astron. Soc. **482**, 52 (2019).
[44] A. B. Joshi, D. Dey, P. S. Joshi, and P. Bambhaniya, Shadow of a naked singularity without photon sphere, Phys. Rev. D **102**, 024022 (2020).
[45] D. Dey, R. Shaikh, and P. S. Joshi, Shadow of nulllike and timelike naked singularities without photon spheres, Phys. Rev. D **103**, 024015 (2021).
[46] V. Perlick, O. Yu. Tsupko, and G. S. Bisnovatyi-Kogan, Black hole shadow in an expanding universe with a cosmological constant, Phys. Rev. D **97**, 104062 (2018).
[47] O. Yu. Tsupko, Z. Fan, and G. S. Bisnovatyi-Kogan, Black hole shadow as a standard ruler in cosmology, Classical Quantum Gravity **37**, 065016 (2020).
[48] S. Vagnozzi, C. Bambi, and L. Visinelli, Concerns regarding the use of black hole shadows as standard rulers, Classical Quantum Gravity **37**, 087001 (2020).
[49] P.-C. Li, M. Guo, and B. Chen, Shadow of a spinning black hole in an expanding universe, Phys. Rev. D **101**, 084041 (2020).
[50] R. Roy and S. Chakrabarti, Study on black hole shadows in asymptotically de Sitter spacetimes, Phys. Rev. D **102**, 024059 (2020).
[51] A. Chowdhuri and A. Bhattacharyya, Shadow analysis for rotating black holes in the presence of plasma for an expanding universe, arXiv:2012.12914.
[52] M. Amir, B. Pratap Singh, and S. G. Ghosh, Shadows of rotating five-dimensional charged EMCS black holes, Eur. Phys. J. C **78**, 399 (2018).
[53] S. Vagnozzi and L. Visinelli, Hunting for extra dimensions in the shadow of M87*, Phys. Rev. D **100**, 024020 (2019).
[54] I. Banerjee, S. Chakraborty, and S. SenGupta, Silhouette of M87*: A new window to peek into the world of hidden dimensions, Phys. Rev. D **101**, 041301 (2020).
[55] S.-F. Yan, C. Li, L. Xue, X. Ren, Y.-F. Cai, D. A. Easson, Y.-F. Yuan, and H. Zhao, Testing the equivalence principle via the shadow of black holes, Phys. Rev. Research **2**, 023164 (2020).
[56] S. E. Gralla, Can the EHT M87 results be used to test general relativity? Phys. Rev. D **103**, 024023 (2021).
[57] C. Li, H. Zhao, and Y.-F. Cai, New test on the Einstein equivalence principle through the photon ring of black holes, arXiv:2102.10888.
[58] Y. Chen, J. Shu, X. Xue, Q. Yuan, and Y. Zhao, Probing Axions with Event Horizon Telescope Polarimetric Measurements, Phys. Rev. Lett. **124**, 061102 (2020).
[59] R. A. Konoplya, Shadow of a black hole surrounded by dark matter, Phys. Lett. B **795**, 1 (2019).
[60] K. Jusufi, M. Jamil, P. Salucci, T. Zhu, and S. Haroon, Black hole surrounded by a dark matter halo in the M87 galactic center and its identification with shadow images, Phys. Rev. D **100**, 044012 (2019).
[61] H. Davoudiasl and P. B. Denton, Ultralight Boson Dark Matter and Event Horizon Telescope Observations of M87*, Phys. Rev. Lett. **123**, 021102 (2019).
[62] R. Roy and U. A. Yajnik, Evolution of black hole shadow in the presence of ultralight bosons, Phys. Lett. B **803**, 135284 (2020).
[63] Saurabh and K. Jusufi, Imprints of dark matter on black hole shadows using spherical accretions, Eur. Phys. J. C **81**, 490 (2021).
[64] A. Abdujabbarov, B. Toshmatov, Z. Stuchlík, and B. Ahmedov, Shadow of the rotating black hole with quintessential energy in the presence of plasma, Int. J. Mod. Phys. D **26**, 1750051 (2017).
[65] X.-X. Zeng and H.-Q. Zhang, Influence of quintessence dark energy on the shadow of black hole, Eur. Phys. J. C **80**, 1058 (2020).
[66] X. Qin, S. Chen, and J. Jing, Image of a regular phantom black hole and its luminosity under spherical accretions, Classical Quantum Gravity **38**, 115008 (2021).
[67] Y. Chen, H.-X. Zhang, T.-C. Ma, and J.-B. Deng, Optical properties of a nonlinear magnetic charged rotating black hole surrounded by quintessence with a cosmological constant, arXiv:2009.03778.
[68] O. Porth *et al.*, The Event Horizon general relativistic magnetohydrodynamic code comparison project, Astrophys. J. Suppl. Ser. **243**, 26 (2019).
[69] R. Narayan, M. D. Johnson, and C. F. Gammie, The shadow of a spherically accreting black hole, Astrophys. J. Lett. **885**, L33 (2019).
[70] J. P. Luminet, Image of a spherical black hole with thin accretion disk, Astron. Astrophys. **75**, 228 (1979).
[71] K. Beckwith and C. Done, Extreme gravitational lensing near rotating black holes, Mon. Not. R. Astron. Soc. **359**, 1217 (2005).
[72] S. E. Gralla, D. E. Holz, and R. M. Wald, Black hole shadows, photon rings, and lensing rings, Phys. Rev. D **100**, 024018 (2019).
[73] V. I. Dokuchaev and N. O. Nazarova, The brightest point in accretion disk and black hole spin: Implication to the image of black hole M87*, Universe **5**, 183 (2019).
[74] J. Peng, M. Guo, and X.-H. Feng, Influence of quantum correction on the black hole shadows, photon rings and lensing rings, arXiv:2008.00657.
[75] K.-J. He, S. Guo, S.-C. Tan, and G.-P. Li, The feature of shadow images and observed luminosity of the Bardeen black hole surrounded by different accretions, arXiv:2103.13664.
[76] A. Eichhorn and A. Held, From a locality-principle for new physics to image features of regular spinning black holes with disks, J. Cosmol. Astropart. Phys. 05 (2021) 073.
[77] G.-P. Li and K.-J. He, Shadows and rings of the Kehagias-Sfetsos black hole surrounded by thin disk accretion, J. Cosmol. Astropart. Phys. 06 (2021) 037.
[78] S. E. Gralla and A. Lupsasca, Lensing by Kerr black holes, Phys. Rev. D **101**, 044031 (2020).
[79] M. D. Johnson *et al.*, Universal interferometric signatures of a black hole's photon ring, Sci. Adv. **6**, eaaz1310 (2020).

[80] S. Hadar, M. D. Johnson, A. Lupsasca, and G. N. Wong, Photon ring autocorrelations, Phys. Rev. D **103**, 104038 (2021).
[81] Remo Ruffini and John A. Wheeler, Introducing the black hole, Phys. Today **24**, No. 1, 30 (1971).
[82] C. A. R. Herdeiro and E. Radu, Asymptotically flat black holes with scalar hair: A review, Int. J. Mod. Phys. D **24**, 1542014 (2015).
[83] S.-W. Wei and Y.-X. Liu, Observing the shadow of Einstein-Maxwell-dilaton-axion black hole, J. Cosmol. Astropart. Phys. 11 (2013) 063.
[84] I. Banerjee, S. Sau, and S. SenGupta, Implications of axionic hair on the shadow of M87*, Phys. Rev. D **101**, 104057 (2020).
[85] L. Amarilla and E. F. Eiroa, Shadow of a Kaluza-Klein rotating dilaton black hole, Phys. Rev. D **87**, 044057 (2013).
[86] S. Dastan, R. Saffari, and S. Soroushfar, Shadow of a Kerr-Sen dilaton-axion black hole, arXiv:1610.09477.
[87] Y. Mizuno, Z. Younsi, C. M. Fromm, O. Porth, M. De Laurentis, H. Olivares, H. Falcke, M. Kramer, and L. Rezzolla, The current ability to test theories of gravity with black hole shadows, Nat. Astron. **2**, 585 (2018).
[88] P. V. P. Cunha, C. A. R. Herdeiro, E. Radu, and H. F. Runarsson, Shadows of Kerr Black Holes with Scalar Hair, Phys. Rev. Lett. **115**, 211102 (2015).
[89] P. V. P. Cunha, J. Grover, C. Herdeiro, E. Radu, H. Runarsson, and A. Wittig, Chaotic lensing around boson stars and Kerr black holes with scalar hair, Phys. Rev. D **94**, 104023 (2016).
[90] P. V. P. Cunha, C. A. R. Herdeiro, E. Radu, and H. F. Runarsson, Shadows of Kerr black holes with and without scalar hair, Int. J. Mod. Phys. D **25**, 1641021 (2016).
[91] R. A. Konoplya and A. Zhidenko, Analytical representation for metrics of scalarized Einstein-Maxwell black holes and their shadows, Phys. Rev. D **100**, 044015 (2019).
[92] R. A. Konoplya, T. Pappas, and A. Zhidenko, Einstein-scalar–Gauss-Bonnet black holes: Analytical approximation for the metric and applications to calculations of shadows, Phys. Rev. D **101**, 044054 (2020).
[93] M. Khodadi, A. Allahyari, S. Vagnozzi, and D. F. Mota, Black holes with scalar hair in light of the Event Horizon Telescope, J. Cosmol. Astropart. Phys. 09 (2020) 026.
[94] Y.-X. Gao and Y. Xie, Gravitational lensing by hairy black holes in Einstein-scalar-Gauss-Bonnet theories, Phys. Rev. D **103**, 043008 (2021).
[95] Q. Gan, P. Wang, H. Wu, and H. Yang, Photon spheres and spherical accretion image of a hairy black hole, Phys. Rev. D **104**, 024003 (2021).
[96] C. A. R. Herdeiro, E. Radu, N. Sanchis-Gual, and J. A. Font, Spontaneous Scalarization of Charged Black Holes, Phys. Rev. Lett. **121**, 101102 (2018).
[97] P. V. P. Cunha, E. Berti, and C. A. R. Herdeiro, Light-Ring Stability for Ultracompact Objects, Phys. Rev. Lett. **119**, 251102 (2017).
[98] R. Shaikh, P. Banerjee, S. Paul, and T. Sarkar, Strong gravitational lensing by wormholes, J. Cosmol. Astropart. Phys. 07 (2019) 028.
[99] N. Tsukamoto, Linearization stability of reflection-asymmetric thin-shell wormholes with double shadows, Phys. Rev. D **103**, 064031 (2021).
[100] M. Guerrero, G. J. Olmo, and D. Rubiera-Garcia, Double shadows of reflection-asymmetric wormholes supported by positive energy thin-shells, J. Cosmol. Astropart. Phys. 04 (2021) 066.
[101] H. M. Reji and M. Patil, Gravitational lensing signature of matter distribution around Schwarzschild black hole, Phys. Rev. D **101**, 064051 (2020).
[102] P. G. S. Fernandes, C. A. R. Herdeiro, A. M. Pombo, E. Radu, and N. Sanchis-Gual, Spontaneous scalarisation of charged black holes: Coupling dependence and dynamical features, Classical Quantum Gravity **36**, 134002 (2019); Erratum, Classical Quantum Gravity **37**, 049501 (2020).
[103] J. L. Blázquez-Salcedo, C. A. R. Herdeiro, J. Kunz, A. M. Pombo, and E. Radu, Einstein-Maxwell-scalar black holes: The hot, the cold and the bald, Phys. Lett. B **806**, 135493 (2020).
[104] D. Astefanesei, C. Herdeiro, A. Pombo, and E. Radu, Einstein-Maxwell-scalar black holes: Classes of solutions, dyons and extremality, J. High Energy Phys. 10 (2019) 078.
[105] P. G. S. Fernandes, C. A. R. Herdeiro, A. M. Pombo, E. Radu, and N. Sanchis-Gual, Charged black holes with axionic-type couplings: Classes of solutions and dynamical scalarization, Phys. Rev. D **100**, 084045 (2019).
[106] D.-C. Zou and Y. S. Myung, Scalarized charged black holes with scalar mass term, Phys. Rev. D **100**, 124055 (2019).
[107] P. G. S. Fernandes, Einstein-Maxwell-scalar black holes with massive and self-interacting scalar hair, Phys. Dark Universe **30**, 100716 (2020).
[108] Y. Peng, Scalarization of horizonless reflecting stars: neutral scalar fields non-minimally coupled to Maxwell fields, Phys. Lett. B **804**, 135372 (2020).
[109] Y. S. Myung and D.-C. Zou, Instability of Reissner-Nordström black hole in Einstein-Maxwell-scalar theory, Eur. Phys. J. C **79**, 273 (2019).
[110] Y. S. Myung and D.-C. Zou, Stability of scalarized charged black holes in the Einstein-Maxwell-scalar theory, Eur. Phys. J. C **79**, 641 (2019).
[111] D.-C. Zou and Y. S. Myung, Radial perturbations of the scalarized black holes in Einstein-Maxwell-conformally coupled scalar theory, Phys. Rev. D **102**, 064011 (2020).
[112] Y. S. Myung and D.-C. Zou, Onset of rotating scalarized black holes in Einstein-Chern-Simons-scalar theory, Phys. Lett. B **814**, 136081 (2021).
[113] Z.-F. Mai and R.-Q. Yang, Stability analysis on charged black hole with nonlinear complex scalar, Phys. Rev. D **104**, 044008 (2021).
[114] D. Astefanesei, C. Herdeiro, J. Oliveira, and E. Radu, Higher dimensional black hole scalarization, J. High Energy Phys. 09 (2020) 186.
[115] Y. S. Myung and D.-C. Zou, Quasinormal modes of scalarized black holes in the Einstein-Maxwell-scalar theory, Phys. Lett. B **790**, 400 (2019).
[116] J. L. Blázquez-Salcedo, C. A. R. Herdeiro, S. Kahlen, J. Kunz, A. M. Pombo, and E. Radu, Quasinormal modes of

hot, cold and bald Einstein-Maxwell-scalar black holes, Eur. Phys. J. C **81**, 155 (2021).
[117] Y. S. Myung and D.-C. Zou, Scalarized charged black holes in the Einstein-Maxwell-scalar theory with two U(1) fields, Phys. Lett. B **811**, 135905 (2020).
[118] Y. S. Myung and D.-C. Zou, Scalarized black holes in the Einstein-Maxwell-scalar theory with a quasitopological term, Phys. Rev. D **103**, 024010 (2021).
[119] H. Guo, X.-M. Kuang, E. Papantonopoulos, and B. Wang, Topology and spacetime structure influences on black hole scalarization, arXiv:2012.11844.
[120] P. Wang, H. Wu, and H. Yang, Scalarized Einstein-Born-Infeld-scalar black holes, Phys. Rev. D **103**, 104012 (2021).
[121] G. Guo, P. Wang, H. Wu, and H. Yang, Scalarized Einstein-Maxwell-scalar black holes in anti–de Sitter spacetime, arXiv:2102.04015,
[122] C.-Y. Zhang, P. Liu, Y. Liu, C. Niu, and B. Wang, Dynamical charged black hole spontaneous scalarization in anti–de Sitter spacetimes, arXiv:2103.13599.
[123] F. Yuan and R. Narayan, Hot accretion flows around black holes, Annu. Rev. Astron. Astrophys. **52**, 529 (2014).
[124] M. D. Johnson *et al.*, Resolved magnetic-field structure and variability near the event horizon of Sagittarius A*, Science **350**, 1242 (2015).
[125] E. F. Eiroa, G. E. Romero, and D. F. Torres, Reissner-Nordstrom black hole lensing, Phys. Rev. D **66**, 024010 (2002).
[126] P. V. P. Cunha and C. A. R. Herdeiro, Stationary Black Holes and Light Rings, Phys. Rev. Lett. **124**, 181101 (2020).
[127] Z.-Y. Tang, Y. C. Ong, and B. Wang, Lux in obscuro II: Photon orbits of extremal AdS black holes revisited, Classical Quantum Gravity **34**, 245006 (2017).
[128] V. Cardoso, L. C. B. Crispino, C. F. B. Macedo, H. Okawa, and Paolo Pani, Light rings as observational evidence for event horizons: Long-lived modes, ergoregions and nonlinear instabilities of ultracompact objects, Phys. Rev. D **90**, 044069 (2014).
[129] M. J Rioja and R. Dodson, Precise radio astrometry and new developments for the next-generation of instruments, Astron. Astrophys. Rev. **28**, 6 (2020).
[130] N. Tsukamoto, Deflection angle of a light ray reflected by a general marginally unstable photon sphere in a strong deflection limit, Phys. Rev. D **102**, 104029 (2020).
[131] N. Tsukamoto, Nonlogarithmic divergence of a deflection angle by a marginally unstable photon sphere of the Damour-Solodukhin wormhole in a strong deflection limit, Phys. Rev. D **101**, 104021 (2020).
[132] A. Meredith Hughes, A. Beasley, and C. Carilli, Next generation very large array: Centimeter radio astronomy in the 2020s, in *International Astronomical Union Circular No. 29* (2015), p. 2255106.
[133] W. Skidmore *et al.*, Thirty Meter Telescope detailed science case: 2015, Res. Astron. Astrophys. **15**, 1945 (2015).
[134] C. Goddi *et al.*, BlackHoleCam: Fundamental physics of the Galactic Center, Int. J. Mod. Phys. D **26**, 1730001 (2017).
[135] C. W. Misner, K. S. Thorne, and J. A. Wheeler, *Gravitation* (W. H. Freeman, San Francisco, 1973).
[136] M. A. Fedderke, P. W. Graham, and S. Rajendran, Axion dark matter detection with CMB polarization, Phys. Rev. D **100**, 015040 (2019).
[137] D. J. Schwarz, J. Goswami, and A. Basu, Geometric optics in the presence of axionlike particles in curved spacetime, Phys. Rev. D **103**, L081306 (2021).